Suppression of internal multiples with a group sparse radon transform for imaging the interior of bone

Gregory Ely, Massachusetts Instiute of Technology, Alison Malcolm, Memorial University of Newfoundland, Guillaume Renaud, French National Center for Scientific Research

SUMMARY

We explore the feasibility of using ultrasound to image through bone. The strong velocity and acoustic impedance contrast between bone and soft tissue like that between salt and sediments, significantly reduces the amount of energy transmitted and generates strong internal multiples. In this paper we present a novel framework for imaging the interior of long bones by using a group sparse hyperbolic radon transform to both denoise and despeckle the resulting image and suppress the internal multiples. Using this technique we demonstrate that it is possible to image the interior of bones despite large velocity contrasts and strong multiples on synthetic and in-vivo data.

INTRODUCTION

Computed tomography (CT) and Magnetic Resonant Imaging (MRI) have primarily been used to image through bone and hard tissue. However, CT involves exposure to ionizing radiation and could be problematic for repeated use and monitoring of chronic conditions. MRI is also a less desirable modality due to its slow acquisition time, bulkiness, and high expense. In this paper we demonstrate that ultrasound can image through bone and measure the inner diameter of long bones, creating the possibility of using ultrasound to study the interior structure of bone.

Bone in the presence of soft tissue generates complex physical phenomena that standard ultrasound techniques cannot accurately image. These techniques typically assume a constant velocity model and single scatterer assumption (Shung, 2015) that break down in the presence of bone. Bone has an acoustic velocity of 3,000-4,100 m/s (Granke et al., 2011), nearly 2-3 times that of soft tissue (1,400 -1700 m/s) (Shung, 2015), causing transmitted waves to steeply refract and generate guided waves. Further complicating imaging, long bones can be anisotropic, with the faster wave propagation being aligned with long axis of the bone (Bernard et al., 2016), introducing ambiguity between the velocity of bone and its thickness. Thus most techniques image on the surface of bone (Beltrame et al., 2012).

The high contrast between soft tissue and bone generates strong internal multiples. Exploration seismology has many methods to address multiples (see Verschuur (2006) for a recent overview). Here we expand upon these techniques to develop a novel group sparse hyperbolic radon transform to suppress multiples in synthetic and in vivo data sets.

ACQUISITION & EXPERIMENT

The data for both the real and synthetic experiments is performed with a synthetic aperture acquisition scheme (Jensen et al., 2006), illustrated in Figure 1. Each ultrasound transducer element is fired individually and all transducers receive signals from all sources. This type of acquisition is analogous to most 2D seismic acquisitions in which a source generates a near spherical wave in the subsurface. Data are recorded on a Philips ATL P4-1 transducer with 96 elements spaced 0.295mm apart sampling 35 μS at a rate of .1μS. Each survey generates a 3D data cube of 96 sources x 96 receivers x 350 time samples.

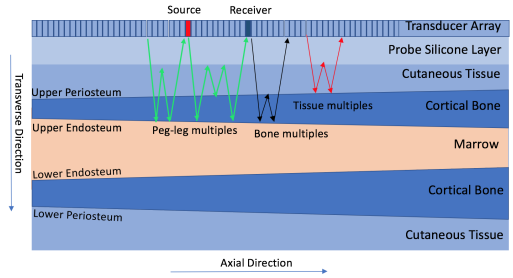

Figure 1: Diagram illustrating the ray paths of the internal multiples and the experimental geometry.

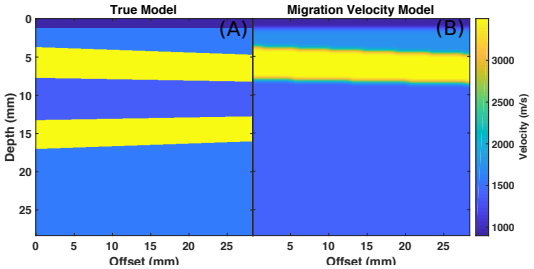

Figure 2: **A:** Synthetic velocity model used to generated finite difference data. **B:** Marrow flood velocity model used for migration of synthetic data.

AXIAL: METHODS & SYNTHETIC

To illustrate the challenges presented by multiples, we simulate a synthetic finite difference acquisition using the velocity model shown in Figure 2A consisting of 96 sources and receivers with the Pysit acoustic finite difference solver Hewett et al. (2013). We generate an image using Kirchhoff migration and the velocity model shown in Figure 2B consisting of only the uppermost section of bone. The resulting migrated image is shown in Figure 3A. From this migration we see that there are numerous internal multiples that corrupt the interpretation of the final image and make it challenging to determine the diameter of the marrow and the lower endosteum interface, the bone and tissue interface shown in Figure 1.

These multiples are particularly apparent when viewed in the data domain. Figure 4A shows a single synthetic gather with

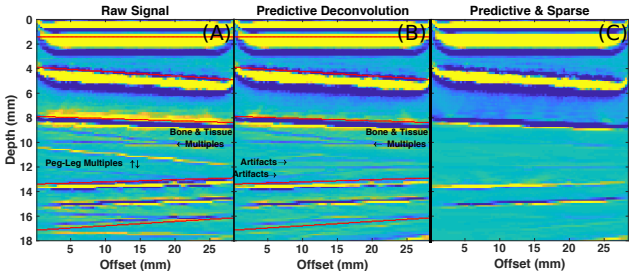

Figure 3: **A:** Migration of the synthetic experiment using velocity model shown in Figure 2B. Numerous multiples are present in the migrated image. **B:** Migration of synthetic data after predictive deconvolution only. Applying only predictive deconvolution introduces numerous artifacts. **C:** migration with sparse hyperbolic denoising and predictive deconvolution. The multiples are significantly reduced and few artifacts remain.

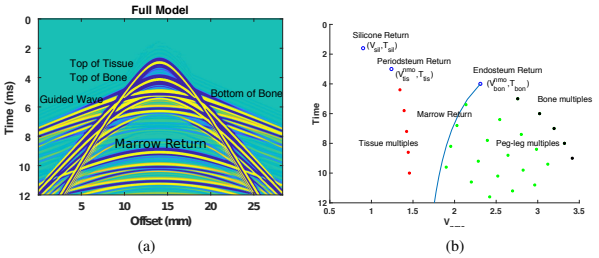

(a) (b)

Figure 4: **A:** Synthetic source gather with direct arrival removed and primaries labeled. There are numerous multiples embedded with the primaries. **B:** Figure shows the nmo velocities and arrival times of the primaries and predicted multiples. The majority of the multiples are separable from the primaries by their moveout.

the direct arrival removed and the primaries labeled. In addition to internal multiples within a single layer (i.e. bone, or cutaneous tissues), there are several peg-leg multiples as illustrated in Figure 1 showing the ray paths of these multiples. We can approximate the arrival time of $t_{nmo}(x)$ of these multiples using the normal moveout equation,

$$t_{nmo}(x) = \sqrt{t_0^2 + \frac{h^2}{V_{nmo}^2}}. \tag{1}$$

Where h is offset and

$$v_{M_{nmo}} = \sqrt{mv_{bone}^2 t_{bone} + nv_{tissue}^2 t_{tissue} + lv_{sil}^2 t_{sil}} \tag{2}$$

$$t_{M_{nmo}} = mt_{bone} + nt_{tissue} + lt_{sil}. \tag{3}$$

Where m,n,l are the number of bounces within the bone, tissue, and silicone layer respectively.

Using this approximation we can predict the arrival time of the multiple for a hypothetical velocity model. Figure 4B shows the estimated primaries (blue circle and solid blue line) as well as the predicted multiple travel time using the approximation given in Equations 3 & 2. From this Figure we see that majority of the multiples can be well separated from the primaries with the exception of the marrow/lower endosteum return (blue line) and one mode of the peg-leg multiples in which the multiple bounces several times within the cutaneous tissue layer. The marrow velocity is slightly slower (1,400 m/s) than the cutaneous tissue velocity (1,500 -1,700 m/s), causing the moveout velocities to vary slightly from the lower endosteum primary. However, these peg-leg multiples have a predictable period of t_{tissue} after the upper endosteum primary. This structure suggests a two step multiple removal approach: first we apply a sparse hyperbolic radon transform to denoise and suppress the majority of the multiples in the moveout velocity domain; second we apply predictive deconvolution to remove the remaining peg-leg multiples.

GUIDED WAVE & NMO VELOCITY ANALYSIS

To suppress the multiples, we first build a simplified velocity model of the upper tissue and bone and estimate tissue and bone nmo velocities and times at each source location. Because the internal multiples are dependent on only $(t_{bone}, t_{tissue}, t_{sil})$ and $(v_{bone}, v_{tissue}, v_{sil})$, these parameters are used for designing thresholds in the sparse hyperbolic radon domain as well as to dictate the optimal length of the predictive deconvolution filter. We first exploit this guided wave to estimate the axial bone velocity and tissue depth. We then use the information extracted from the guided wave to narrow our automatic selection of the upper endosteum depth and transverse bone velocity.

The velocity contrast between bone and tissue (4,000 m/s vs 1,550 m/s) is large enough to generate a strong guided wave (see Figure 4A) that we can exploit to estimate bone depth and axial velocity. To measure this velocity, we perform a slant stack semblance velocity analysis for the 10 left-most and 10 right-most source gathers. To each of the gathers we first apply a mute to remove the direct arrival and then calculate the semblance along a range of velocities and $t = 0$. We then select the velocity and $t = 0$ intercept with the highest semblance value and average them to calculate an effective velocity in the up dip and down direction V_u and V_d and the corresponding t_0 intercepts t_u, and t_d. We then invert for dip angle, θ,

$$V_h = \frac{V_{tis}}{\sin(\frac{1}{2}(\sin^{-1}(\frac{V_{tis}}{V_d}) - \sin^{-1}(\frac{V_{tis}}{V_u})))} \tag{4}$$

and axial bone velocity,

$$\theta = \frac{1}{2}(\sin^{-1}(\frac{V_{tis}}{V_d}) - \sin^{-1}(\frac{V_{tis}}{V_u})). \tag{5}$$

Because the bone is anisotropic with the axial velocity being larger than the transverse velocity, the recovered axial velocity can be used as an upper limit when searching for the transverse velocity. In addition, the values of t_u and t_d can be used to guide our automatic selection of $t_{bone_{nmo}}$ in nmo semblance space.

To estimate the transverse bone velocity, we perform an nmo semblance analysis in the common midpoint domain for 30

midpoint gathers centered within the array. To mitigate the effects of anisotropy, we perform the nmo semblance analysis with 10mm of offset. From the previous guided wave analysis, we linearly interpolate t_u and t_d to roughly estimate t_0 at each midpoint gather and take the largest peak 1.5-6.5 microseconds after the upper periosteum arrival and between 200 and 1,750 m/s less than the estimated head wave velocity. We then perform a weighted linear least squared fit to more accurately estimate $v_{bone_{nmo}}$ and $t_{bone_{nmo}}$.

GROUP SPARSE HYPERBOLIC RADON

The nmo semblance analysis in the previous section provides enough information to build an accurate model of internal multiple travel time and effective move-out velocities. We can now use the estimated nmo velocities and arrival times to construct a filter in the hyperbolic radon domain.

From Figure 4B and the discussion in the previous section, we demonstrated that the majority of the multiples can be separated in the nmo velocity and time domain with only the peg-leg multiples having a similar nmo velocity as the expected marrow return. We now present a framework that uses the signal's compactness in the nmo velocity time domain to suppress multiples and denoise the gathers.

We first construct a dictionary of basis function Γ such that an observed gather D can be written as the summation of only a few basis functions. In the acquisition geometry the reflectors of interest are relatively simple and can be well approximated by a few planar reflectors with minimal dip. Under these assumptions, the reflectors' travel time can be well approximated by Equation 1. We let Γ describe the noiseless signal at a single receiver at offset, x_i, for a planar reflector with nmo time t_j and nmo velocity v_k from an impulsive source,

$$\Gamma^{i,j,k} = \begin{cases} \delta(t_{nmo}(t_j, x_i, v_k)) & \text{if } i' = i \\ \vec{0} & \text{if } i' \neq i. \end{cases} \tag{6}$$

Therefore the reflection from an impulsive source $D_\delta(t_j, v_k)$ with nmo time t_j and nmo velocity v_k can be written as the weighted sum,

$$D_\delta(t_j, v_k) = \sum_{i=0}^{i=N_x} w_i \Gamma^{i,t_j,v_k} \tag{7}$$

where w_i is amplitude of the reflection at each offset index. Using Equation 6 we construct a matrix of propagators Φ where each column of Φ corresponds to a single propagator given by Equation 6. We can rewrite this in matrix notation as,

$$\Phi = [\Gamma^{i,1,k}(:), \Gamma^{i,2,k}(:), ...\Gamma^{N_t,N_t,N_v}(:)], \tag{8}$$

indexed along three different dimensions: nmo velocity, nmo time, and receiver index. The observed data can then be written as the weighted sum of the dictionary elements,

$$D = \Phi X(:) + N \tag{9}$$

where X is a 3 dimensional weighting matrix, N is Gaussian noise, and $(:)$ is the vectorization operator that converts an N-dimensional array to a vector. From Equation 7 the signal for an impulsive source will be group sparse under equation 9 in that all of the non-zero dictionary coefficients w_i will lie on the single column with the common nmo velocity and nmo time index. Therefore the support, or non-zero elements of a given gather of n_D traces D of size $n_t \times n_D$ is well described by the combination of a few combinations of nmo velocities and nmo times. We exploit this column-wise or group sparsity by framing the denoising inverse problem as a regularized convex optimization problem (Tropp, 2006),

$$\hat{X} = \min_{\hat{x}} |\Phi X(:) - B|_2^2 + \lambda |X|_{1,2}. \tag{10}$$

In which we minimize the sum of the misfit between the observed data and $\ell_{1,2}$ norm along the receiver axis of dictionary where λ is the sparse tuning parameter determining the trade off between minimizing the misfit and the group sparsity of the dictionary coefficients. This group sparse penalization method is used by Ely and Aeron (2013) to localize micro-seismic and by to Aeron et al. (2011) to extract dispersion curves.

Under this construction the dictionary can be thought of a generalized radon transform through the offset and time dimension of the data and is extremely large and sparse making the application of Φ and Φ^t to a vector very cheap. Variations of sparse radon domain are used throughout geophysics to denoise and interpolate data, (Li and Li, 2016; Schonewille et al., 2007; Lu, 2013; Trad et al., 2003). However the Φ dictionary does not have any particular structure and it would be computational infeasible to store its LU factorization because the decomposed matrices would be dense. Because of this, methods that rely on LU or partial factorizations, such as ADMM (Goldstein et al., 2014), are computational infeasible and we instead use FISTA (Beck and Teboulle, 2009), Algorithm 1, that only requires the application of Φ and Φ^t to a vector. Figure 5 shows a synthetic source gather with and without the group sparse denoising. After the group sparse radon procedure has been applied, the multiples are significantly reduced.

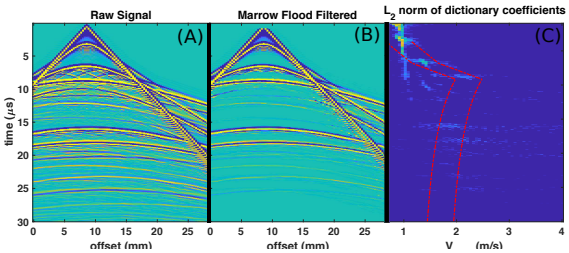

Figure 5: **A:** Original synthetic finite difference source gather. **B:** synthetic finite difference trace with hyperbolic denoising and multiple removal. **C:** The ℓ_2 norm of the radon dictionary elements in which the gather is sparse. Red dashed lines show the edges of mute in this domain used to suppress the multiples.

Predictive Deconvolution

Once the sparse hyperbolic radon filter has been applied to the data, the remaining traces only contain the peg-leg multiples with period of t_{tissue} and moveout velocity nearly identical to the marrow velocity. To remove the remaining multiples we first apply an nmo correction Yilmaz (2001) to flatten the raw

Algorithm 1 FISTA: solves $\min_X ||\Phi X - B||_2^2 + \lambda \mathbf{F}(X)$ (Eq. 10)

1: $X = \mathbf{0}$ //Initialize variables.
2: $k = 1$
3: **while** true **do**
4: $X_{old} = X; k = k+1;$
5: $U = X + \frac{k-1}{k+2}(X - X_{old})$ //Interpolation
6: $Z = U - \frac{1}{\rho}\Phi^T(\Phi U - B)$ //Gradient calculation
7: $X = \min_X \frac{1}{2}||X - Z||_2^2 + \frac{\lambda}{\rho}\sum_{N_x}^{i=1}||Z(:,i)||_2$ //Apply shrinkage operator
8: **end while**

source gathers and apply a tapered mute 1 μS before the predicted upper endosteum return such that the upper periosteum and silicone primaries are not contained in the gathers, because applying predictive deconvolution to the raw data would introduce erroneous reflectors t_{tissue} after the primaries, as shown in Figure 3B. We then apply an inverse nmo filter to return the data to the original domain and stitch the data together with the raw data prior to the endosteum arrival. Figure 3C shows the synthetic migration with predictive deconvolution and hyperbolic denoise applied to the data. Nearly all of the multiple energy is suppressed in the final image.

Narrow Offset Migration

Although in this acquisition geometry the bone is anisotropic with the fast axis aligned with the axial direction of the bone, we can mitigate the effects of anisotropy by migrating the data and updating the image with limited offset. This does introduce an ambiguity between the thickness of the marrow and the vertical bone velocity. However, imaging the marrow structure and internal radius of the bone is not heavily dependent on the bone velocity and an isotropic model is sufficient.

RESULTS: IN-VIVO

We now apply our velocity analysis and multiple removal framework to an in-vivo data set of the radius bone in a human forearm. Figure 6 shows the Kirchoff migration performed on the raw data without any denoising or multiple removal. The image is shown both with in decibel scale for the envelope detected data and a linear scale adjusted to highlight the amplitude of the reflectors within the marrow. Although the lower endosteum interface is barely visible in the raw image there is significant speckle present within the marrow embedded within numerous coherent reflectors and it is challenging to determine the correct reflector.

We first apply our semblance analysis to extract an axial bone velocity of 3,990 m/s and transverse/narrow offset velocity of 3,850 m/s. Figure 7A shows a raw single source gather. The hyperbolic radon domain significantly suppresses the noise and enhances the coherent reflectors (Figure 7B) and predictive deconvolution decreases the energy of the peg-leg multiple visible at 11μS (Figure 7C). A velocity model consisting of only the upper bone and marrow velocity below is used for the migration similar to the one shown in Figure 2B. After applying the sparse hyperbolic radon transform, the speckle is significantly reduced and only a few coherent reflectors are present

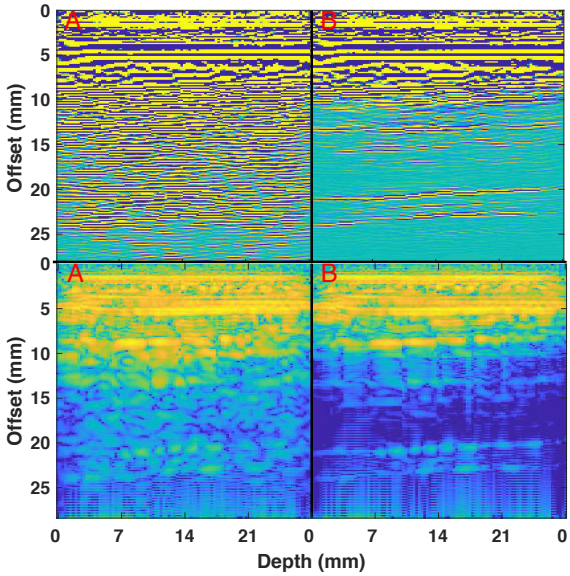

Figure 6: The upper panels are shown in linear scale tuned to highlight the reflectors within the marrow and the lower panels show the envelope detected image with 50dB of dynamic range. **A:** Migration with raw data. **B:** Migration with hyperbolic radon denoising. **C:**

in the image, Figure 6B. Applying the predictive deconvolution decreases the amplitude of the peg-leg multiple and further eases interpretation of images such that it could be possible to automatically select the marrow interface visible at approximately 20mm depth.

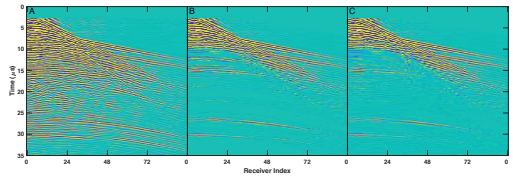

Figure 7: **A:** Raw in-vivo source gather. **B:** in-vivo source gather with sparse radon denoising. **C:** in-vivo source gather with sparse hyperbolic radon denoising and predictive deconvolution.

CONCLUSION

In this paper we successfully demonstrated the feasibility of imaging the interior of long bones by leveraging numerous seismic techniques. To do so we introduced a novel method for suppressing multiples and speckle reduction using the group sparse hyperbolic radon transform.

ACKNOWLEDGMENTS

This material is based upon work supported by MITs Earth Resources Laboratory. Alison Malcolm is grateful for financial support from Chevron, NSERC under grants IRCPJ 491051-14 & RGPIN-2016-04415 and InnovateNL under grant 5405.1085.104.

REFERENCES

Aeron, S., S. Bose, H.-P. Valero, and V. Saligrama, 2011, Broadband dispersion extraction using simultaneous sparse penalization: IEEE Transactions on Signal Processing, **59**, 4821–4837.

Beck, A., and M. Teboulle, 2009, A fast iterative shrinkage-thresholding algorithm for linear inverse problems: SIAM journal on imaging sciences, **2**, 183–202.

Beltrame, V., R. Stramare, N. Rebellato, F. Angelini, A. C. Frigo, and L. Rubaltelli, 2012, Sonographic evaluation of bone fractures: a reliable alternative in clinical practice?: Clinical imaging, **36**, 203–208.

Bernard, S., J. Schneider, P. Varga, P. Laugier, K. Raum, and Q. Grimal, 2016, Elasticity–density and viscoelasticity–density relationships at the tibia mid-diaphysis assessed from resonant ultrasound spectroscopy measurements: Biomechanics and modeling in mechanobiology, **15**, 97–109.

Ely, G., and S. Aeron, 2013, Methods for large scale hydraulic fracture monitoring: Computational Advances in Multi-Sensor Adaptive Processing (CAMSAP), 2013 IEEE 5th International Workshop on, IEEE, 272–275.

Goldstein, T., B. O'Donoghue, S. Setzer, and R. Baraniuk, 2014, Fast alternating direction optimization methods: SIAM Journal on Imaging Sciences, **7**, 1588–1623.

Granke, M., Q. Grimal, A. Saïed, P. Nauleau, F. Peyrin, and P. Laugier, 2011, Change in porosity is the major determinant of the variation of cortical bone elasticity at the millimeter scale in aged women: Bone, **49**, 1020–1026.

Hewett, R., L. Demanet, and the PySIT Team, 2013, PySIT: Python seismic imaging toolbox v0.5. (Release 0.5).

Jensen, J. A., S. I. Nikolov, K. L. Gammelmark, and M. H. Pedersen, 2006, Synthetic aperture ultrasound imaging: Ultrasonics, **44**, e5–e15.

Li, Z., and Z. Li, 2016, Accelerated and automatic sparse parabolic radon transform in the mixed frequency-time domain with alternating split bregman algorithm, *in* SEG Technical Program Expanded Abstracts 2016: Society of Exploration Geophysicists, 4524–4528.

Lu, W., 2013, An accelerated sparse time-invariant radon transform in the mixed frequency-time domain based on iterative 2d model shrinkage: Geophysics, **78**, V147–V155.

Schonewille, M., P. Aaron, and T. Allen, 2007, Applications of time-domain high-resolution radon demultiple: ASEG Extended Abstracts, **2007**, 1–5.

Shung, K. K., 2015, Diagnostic ultrasound: Imaging and blood flow measurements: CRC press.

Trad, D., T. Ulrych, and M. Sacchi, 2003, Latest views of the sparse radon transform: Geophysics, **68**, 386–399.

Tropp, J. A., 2006, Algorithms for simultaneous sparse approximation. part ii: Convex relaxation: Signal Processing, **86**, 589–602.

Verschuur, D. J., 2006, Seismic multiple removal techniques: Past, present and future: EAGE publications Netherlands.

Yilmaz, Ö., 2001, Seismic data analysis: Processing, inversion, and interpretation of seismic data: Society of exploration geophysicists.